J. Fluid Mech. (2011), *vol.* 688, *pp.* 569–590.
doi:10.1017/jfm.2011.405

Linear stability of compressible flow in a streamwise corner

Oliver T. Schmidt† and Ulrich Rist

Institut für Aerodynamik und Gasdynamik, Universität Stuttgart, Pfaffenwaldring 21, 70569 Stuttgart, Germany

(Received 20 May 2011; revised 20 May 2011; accepted 17 September 2011; first published online 4 November 2011)

The linear stability of the compressible flow in a streamwise corner is studied. The steady laminar mean flow is obtained as a solution to the parabolized Navier–Stokes equations with the asymptotic cross-flow velocity enforced on the far-field boundaries via a sponge region and was found to be in good agreement with the corresponding self-similar solution. The eigenvalue problem of linear stability theory is solved for base flows at three different Mach numbers representing the incompressible limit ($Ma = 0.01$), the subsonic ($Ma = 0.95$) and the supersonic ($Ma = 1.5$) velocity regime. Particular attention is given to the subject of wave obliqueness. Owing to the break of periodicity by the opposing wall the exact spanwise wavenumbers and associated phase angles resolved in the computational domain are not known *a priori*. We address this problem by imposing different phase angles on the far-field boundaries to obtain the critical values of the Reynolds number, streamwise wavenumber and spanwise wavenumber from a three-dimensional solution space. The stability characteristics of the different types of modes present in the spectrum are discussed. An inviscid corner mode with odd-symmetry not present in the subsonic regime and with a higher amplification rate than its symmetric counterpart is identified in the supersonic case. Acoustic modes are found in an enlarged computational domain and categorized with respect to speed, symmetry and wall-boundedness, among them an acoustic corner mode.

Key words: boundary layer stability, compressible boundary layers

1. Introduction

The flow along a corner formed by two perpendicular semi-infinite flat plates as depicted in figure 1 has been the focus of numerous numerical and experimental studies in the past and serves as a generic model geometry for the wing–fuselage intersection of an airplane, rotor–hub junctions or supersonic engine inlets. Here, x is the streamwise coordinate, y and z the spanwise coordinates with the corner located at $y = z = 0$. The leading edge of the corner is located at $x = 0$. At distances far away from the opposing plate the flow resembles the two-dimensional flat-plate scenario in terms of streamwise velocity, wall-normal velocity, density and temperature as indicated by the streamwise velocity profiles. In addition, a cross-flow velocity component is induced by the displacement effect of the opposing wall in that limit.

† Email address for correspondence: o.schmidt@iag.uni-stuttgart.de

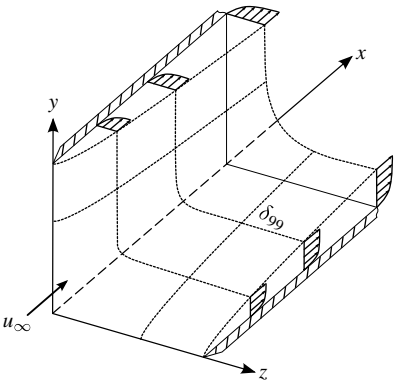

FIGURE 1. Schematic diagram of flow in a streamwise corner.

After early attempts by Carrier (1947) it was up to Rubin (1966) to derive a full set of equations governing the laminar incompressible self-similar corner-flow problem using matched asymptotic expansions. The solution of the asymptotic secondary cross-flow was identified as the far-field boundary condition necessary for the calculation of the internal flow field. A more detailed study of the asymptotic behaviour by Pal & Rubin (1971) followed. In the same year, Rubin & Grossman (1971) obtained a first numerical solution to the corner-flow equations. Further work on the incompressible equations included reformulation in curvilinear coordinates (Zamir 1970), development of more efficient numerical algorithms (Ghia & Davis 1974*b*), mapping of the far-field boundaries to true infinity (Ghia 1975), extension to arbitrary angles (Barclay & Ridha 1980), inclusion of a non-zero streamwise pressure gradient (Ridha 1992), wall suction (Barclay & El-Gamal 1983, 1984) and combined free and forced convection (Ridha 2002). A notable feature of the governing equations is the existence of a dual solution for non-zero streamwise pressure gradients found by Ridha (1992). The two existing solutions are distinguished by different values of wall shear for a given pressure gradient parameter and referred to as upper and lower branch solutions. A comprehensive study on the dual solutions was conducted by (Duck & Dhanak 1996). The effect of compressibility was introduced by Weinberg & Rubin (1972) for a model fluid at unity Prandtl number. Mikhail & Ghia (1978) dropped the model fluid assumption and calculated solutions for different wall and free stream temperatures with far-field boundary conditions imposed at true infinity. Self-similarity and shock-free flow were assumed herein.

Along with the theoretical/numerical efforts, experimental investigations were conducted by different authors. Particularly notable is the work by Zamir (1981) who compares his results with numerous previous experimental studies (Nomura 1962; Zamir & Young 1970; Barclay 1973; El-Gamal & Barclay 1978; Zamir & Young 1979) and theory. It is concluded from experimental evidence that the corner layer is stable for local Reynolds numbers greater than about 10^4 only with some favourable pressure gradient in the streamwise direction. At distances far from the corner region the flow shows stability characteristics similar to the two-dimensional flat-plate scenario. However, a high sensitivity to perturbations is attested to the boundary layer in the vicinity of the corner. This results in a critical Reynolds number that is about one order of magnitude lower as compared with the two-dimensional flat plate. Departure from similarity manifests in an outward bulge of the velocity contours on the plane of symmetry which was also theoretically ascertained by Nomura (1982).

After transition to turbulence, reversal of the cross-flow direction from outgoing to incoming was observed by Zamir & Young (1970).

In the beginning, stability calculations were restricted to one-dimensional computations using linear stability theory (LST) for velocity profiles along the blending boundary layer between the corner and the far-field region. Lakin & Hussaini (1984) pioneered this approach, followed by Dhanak (1992, 1993) with improved boundary conditions and by Duck & Dhanak (1996) who included the effect of a streamwise pressure gradient. Balachandar & Malik (1993) were the first to perform a two-dimensional stability analysis for the inviscid limit. Solutions for the viscous problem were obtained by Parker & Balachandar (1999) including the effect of pressure gradients and spanwise wave obliqueness on amplification rates. The critical Reynolds number was found to be somewhat higher than for the two-dimensional flat-plate scenario which contrasts observations made in experiment. Besides viscous modes of varying spanwise wavenumbers, an inviscid even-symmetric corner mode was identified. However, the inviscid corner mode exhibits no temporal amplification. The existence of unstable inviscid modes in the spectrum suggested by an inviscid stability analysis (Balachandar & Malik 1993) could not be supported. By solving the parabolized stability equations (PSE) in their analysis, Galionis & Hall (2005) were able to drop the parallel-flow assumption within a spatial framework. The authors also readdress the influence of domain truncation on amplification rates and emphasize the increasing importance of the inviscid mode with an increasing adverse pressure gradient. Amplification rates were found in good agreement with linear theory for small wave obliqueness angles. Most recently, Alizard, Robinet & Rist (2010) analysed the sensitivity of incompressible corner flow with respect to base-flow variations. Their study reveals a significant reduction of the critical Reynolds number for only slight base-flow deviations.

The present study examines the linear stability properties of corner flow up to a Mach number of 1.5 with adiabatic walls. Special attention is given to the influence of compressibility effects and wave obliqueness. It is organized as follows. The calculation of the laminar base flow by means of the parabolized Navier–Stokes equations is addressed in § 2, followed by the description of the method and discussion of the results of the linear stability analysis in § 3. Finally, a brief summary and prospective view is given in § 4.

2. Base flow

The compressible flow in an axial corner with zero streamwise pressure gradient is computed as a solution to the parabolized Navier–Stokes (PNS) equations. The self-similar solution (Weinberg & Rubin 1972; Mikhail & Ghia 1978) can be obtained by applying the appropriate asymptotic boundary conditions and coordinate transformation in the transversal planes within the PNS method and converging the solution. For a detailed review of the PNS approach the reader is referred to Rubin & Tannehill (1992) and Tannehill, Anderson & Pletcher (1997, pp. 537–617). In the following, the Cartesian velocity components u, v, w are non-dimensionalized by the potential velocity u_∞, density ρ and temperature T by their respective free stream values (subscript ∞) and length scales by the local incompressible displacement thickness

$$\delta_1 = \int_0^\infty \left(1 - \frac{u}{u_\infty}\right) \mathrm{d}y. \tag{2.1}$$

The incompressible definition of the displacement thickness is employed as the influence of the corner on the density field can lead to a non-zero integrand outside the boundary layer for the compressible definition. The following non-dimensional numbers are used to describe the flow:

$$Re = \frac{\rho_\infty u_\infty \delta_1}{\mu_\infty}, \quad Pr = \frac{c_p \mu_\infty}{k_\infty}, \quad Ma = \frac{u_\infty}{a_\infty}. \tag{2.2}$$

Here, Re is the local Reynolds number, Pr the Prandtl number and Ma the global Mach number; μ_∞, c_p, k_∞ and a_∞ denote the dynamic viscosity, heat capacity at constant pressure, thermal conductivity and speed of sound, respectively. The pressure p is non-dimensionalized by twice the dynamic pressure $\rho_\infty u_\infty^2$. An ideal gas governed by the equation of state

$$p = \rho R T \tag{2.3}$$

is assumed. Pressure, density and temperature are related through the ideal gas constant R. The dependence of viscosity on temperature is given by Sutherland's law

$$\mu(T) = \mu_r T^{3/2} \frac{1 + T_r}{T + T_r}. \tag{2.4}$$

Throughout this study, the following free stream values and fluid properties are employed corresponding to dry air at standard conditions:

$$p_\infty = 1.01325 \times 10^5 \text{ Pa}, \quad T_\infty = 293.15 \text{ K}, \quad Pr = 0.714, \tag{2.5a}$$

$$\gamma = 1.4, \quad c_p = 1005 \text{ J kg}^{-1} \text{ K}^{-1}, \quad R = 287 \text{ J kg}^{-1} \text{ K}^{-1}, \tag{2.5b}$$

$$\mu_r = 1.735 \times 10^{-5} \text{ kg m}^{-1} \text{ s}^{-1}, \quad T_r = 280 \text{ K}. \tag{2.5c}$$

The heat capacity ratio $\gamma = c_p/c_v$ is the ratio of heat capacity at constant pressure c_p to heat capacity at constant volume c_v.

2.1. *PNS equations*

Dropping the unsteady and all viscous terms containing partial derivatives with respect to the streamwise coordinate x from the full Navier–Stokes equations for a compressible fluid results in the steady PNS equations. The resulting set of equations for continuity, streamwise momentum, y momentum, z momentum and energy reads

$$\frac{\partial \rho u}{\partial x} + \frac{\partial \rho v}{\partial y} + \frac{\partial \rho w}{\partial z} = 0, \tag{2.6}$$

$$\rho u \frac{\partial u}{\partial x} + \rho v \frac{\partial u}{\partial y} + \rho w \frac{\partial u}{\partial z} = -\frac{\partial p}{\partial x} + \frac{\partial}{\partial y}\left(\mu \frac{\partial u}{\partial y}\right) + \frac{\partial}{\partial z}\left(\mu \frac{\partial u}{\partial z}\right), \tag{2.7}$$

$$\begin{aligned} \rho u \frac{\partial v}{\partial x} + \rho v \frac{\partial v}{\partial y} + \rho w \frac{\partial v}{\partial z} = &-\frac{\partial p}{\partial y} + \frac{4}{3}\frac{\partial}{\partial y}\left(\mu \frac{\partial v}{\partial y}\right) + \frac{\partial}{\partial z}\left(\mu \frac{\partial v}{\partial z}\right) \\ &+ \frac{\partial}{\partial z}\left(\mu \frac{\partial w}{\partial y}\right) - \frac{2}{3}\frac{\partial}{\partial y}\left(\mu \frac{\partial w}{\partial z}\right), \end{aligned} \tag{2.8}$$

$$\begin{aligned} \rho u \frac{\partial w}{\partial x} + \rho v \frac{\partial w}{\partial y} + \rho w \frac{\partial w}{\partial z} = &-\frac{\partial p}{\partial z} + \frac{4}{3}\frac{\partial}{\partial z}\left(\mu \frac{\partial w}{\partial z}\right) + \frac{\partial}{\partial y}\left(\mu \frac{\partial w}{\partial y}\right) \\ &+ \frac{\partial}{\partial y}\left(\mu \frac{\partial v}{\partial z}\right) - \frac{2}{3}\frac{\partial}{\partial z}\left(\mu \frac{\partial v}{\partial y}\right), \end{aligned} \tag{2.9}$$

$$\rho u c_v \frac{\partial T}{\partial x} + \rho v c_v \frac{\partial T}{\partial y} + \rho w c_v \frac{\partial T}{\partial z} = -p\left(\frac{\partial u}{\partial x} + \frac{\partial v}{\partial y} + \frac{\partial w}{\partial z}\right) + \frac{\partial}{\partial y}\left(k\frac{\partial T}{\partial y}\right) + \frac{\partial}{\partial z}\left(k\frac{\partial T}{\partial z}\right) + \mu\left[\left(\frac{\partial u}{\partial y}\right)^2 + \left(\frac{\partial u}{\partial z}\right)^2 + \left(\frac{\partial w}{\partial y} + \frac{\partial v}{\partial z}\right)^2\right] + \frac{4}{3}\mu\left[\left(\frac{\partial v}{\partial y}\right)^2 + \left(\frac{\partial w}{\partial z}\right)^2 - \frac{\partial v}{\partial y}\frac{\partial w}{\partial z}\right]. \tag{2.10}$$

The variables ρ, u, v, w and T denote density, the three Cartesian velocity components and temperature, respectively. By omitting the streamwise pressure gradient and linearization by lagging of coefficients the PNS equations are recast in matrix form

$$\boldsymbol{A}\frac{\partial \boldsymbol{q}}{\partial x} + \boldsymbol{B}\frac{\partial \boldsymbol{q}}{\partial y} + \boldsymbol{C}\frac{\partial \boldsymbol{q}}{\partial z} = 0 \tag{2.11}$$

for the solution vector $\boldsymbol{q} = [\rho, u, v, w, T]^{\mathrm{T}}$ of primitive variables and the coefficient matrices

$$\boldsymbol{A} = \begin{bmatrix} u & \rho & 0 & 0 & 0 \\ 0 & \rho u & -\frac{\partial \mu}{\partial y} & -\frac{\partial \mu}{\partial z} & 0 \\ 0 & \frac{2}{3}\frac{\partial \mu}{\partial y} & \rho u & 0 & 0 \\ 0 & \frac{2}{3}\frac{\partial \mu}{\partial z} & 0 & \rho u & 0 \\ 0 & p & 0 & 0 & c_v \rho u \end{bmatrix}, \tag{2.12a}$$

$$\boldsymbol{B} = \begin{bmatrix} v & 0 & \rho & 0 & 0 \\ 0 & \rho v - \frac{\partial \mu}{\partial y} - \mu\frac{\partial}{\partial y} & 0 & 0 & 0 \\ RT & 0 & \rho v - \frac{4}{3}\mu\frac{\partial}{\partial y} - \frac{4}{3}\frac{\partial \mu}{\partial y} & -\frac{1}{6}\mu\frac{\partial}{\partial z} - \frac{\partial \mu}{\partial z} & \mathrm{R}\rho \\ 0 & 0 & -\frac{1}{6}\mu\frac{\partial}{\partial z} + \frac{2}{3}\frac{\partial \mu}{\partial z} & \rho v - \frac{\partial \mu}{\partial y} - \mu\frac{\partial}{\partial y} & 0 \\ 0 & -\mu\frac{\partial u}{\partial y} & \frac{2}{3}\mu\frac{\partial w}{\partial z} + p - \frac{4}{3}\mu\frac{\partial v}{\partial y} & -\mu\left(\frac{\partial w}{\partial y} + \frac{\partial v}{\partial z}\right) & -k\frac{\partial}{\partial y} + c_v\rho v - \frac{\partial k}{\partial y} \end{bmatrix} \tag{2.12b}$$

and

$$\boldsymbol{C} = \begin{bmatrix} w & 0 & 0 & \rho & 0 \\ 0 & \rho w - \frac{\partial \mu}{\partial z} - \mu\frac{\partial}{\partial z} & 0 & 0 & 0 \\ 0 & 0 & \rho w - \frac{\partial \mu}{\partial z} - \mu\frac{\partial}{\partial z} & -\frac{1}{6}\mu\frac{\partial}{\partial y} + \frac{2}{3}\frac{\partial \mu}{\partial y} & 0 \\ RT & 0 & -\frac{1}{6}\mu\frac{\partial}{\partial y} - \frac{\partial \mu}{\partial y} & \rho w - \frac{4}{3}\mu\frac{\partial}{\partial z} - \frac{4}{3}\frac{\partial \mu}{\partial z} & \mathrm{R}\rho \\ 0 & -\mu\frac{\partial u}{\partial z} & -\mu\left(\frac{\partial v}{\partial y} + \frac{\partial w}{\partial z}\right) & \frac{2}{3}\mu\frac{\partial v}{\partial y} + p - \frac{4}{3}\mu\frac{\partial w}{\partial z} & -k\frac{\partial}{\partial z} + c_v\rho w - \frac{\partial k}{\partial z} \end{bmatrix}. \tag{2.12c}$$

Superscript T refers to the vector transpose. The system of (2.11) can be solved by space-marching transversal planes in the parabolized direction. This procedure is valid for flows where gradients in the streamwise directions are expected to be small compared with cross-flow gradients as in boundary-layer-type flows (Tannehill *et al.* 1997, pp. 537–541). A pseudospectral collocation method based on Chebyshev

polynomials is used to discretize the equations (details on the method are given in § 2.3). Within the pseudospectral framework, derivatives in the transversal directions are replaced by Chebyshev differentiation matrices $\boldsymbol{D_y}$ and $\boldsymbol{D_z}$ (see § 2.3). In addition, a sponge zone term (Bodony 2006) is introduced in the discretized equation to account for the algebraic approach of the flow field towards the asymptotic far-field solution $\boldsymbol{q}_r$ (see § 2.2). The resulting discretized form of the PNS is given by

$$\boldsymbol{A}\left(\frac{\boldsymbol{q}^{(i+1)}-\boldsymbol{q}^{(i)}}{\Delta x}+\mathrm{O}(\Delta x)\right)+\boldsymbol{B}\boldsymbol{D_y}\boldsymbol{q}^{(i+1)}+\boldsymbol{C}\boldsymbol{D_z}\boldsymbol{q}^{(i+1)}-\sigma(\boldsymbol{q}^{(i+1)}-\boldsymbol{q}_r)=0. \quad (2.13)$$

A first-order accurate implicit Euler method is used to spatially advance the solution from $\boldsymbol{q}^{(i)}$ to $\boldsymbol{q}^{(i+1)}$ over a distance Δx. By collecting all terms containing $\boldsymbol{q}^{(i+1)}$ in one operator $\boldsymbol{L}$ and all other terms in a right-hand side vector $\boldsymbol{r}$

$$\left[\frac{1}{\Delta x}\boldsymbol{A}+\boldsymbol{B}\boldsymbol{D_y}+\boldsymbol{C}\boldsymbol{D_z}-\sigma\right]\boldsymbol{q}^{(i+1)}=\frac{1}{\Delta x}\boldsymbol{A}\boldsymbol{q}^{(i)}-\sigma\boldsymbol{q}_r \quad (2.14)$$

we obtain the linear system

$$\boldsymbol{L}\boldsymbol{q}^{(i+1)}=\boldsymbol{r}. \quad (2.15)$$

For a computational domain of $N\times N$ collocation points, the overall size of the linear operator is $5N^2$. Equation (2.15) is solved using a standard algorithm for large sparse systems (Davis 2006).

2.2. *Boundary and initial conditions*

Boundary conditions are enforced in a strong sense by modification of the corresponding rows of $\boldsymbol{L}$ and $\boldsymbol{r}$. Under the assumption of solid no-slip walls with adiabatic heat transfer, the following boundary conditions hold

$$u=v=w=\frac{\partial T}{\partial n}=0 \quad (2.16)$$

for the three velocity components and the temperature. Here n corresponds to the surface normal direction. For a zero wall-normal pressure gradient $\partial p/\partial n=0$ commonly assumed in boundary-layer-type flows, the wall density can be calculated from the discretized version of the equation of state for an ideal gas (2.3)

$$\rho^{(i)}\frac{\partial T^{(i+1)}}{\partial n}+T^{(i)}\frac{\partial \rho^{(i+1)}}{\partial n}=0 \quad (2.17)$$

linearized consistently with (2.11).

The far-field boundary imposes a challenging task as only algebraic approach of the cross-flow towards the asymptotic solution can be expected (Rubin 1966; Weinberg & Rubin 1972). This asymptotic behaviour is accounted for by the combined use of a homogeneous Neumann boundary condition

$$\frac{\partial \boldsymbol{q}}{\partial n}=0 \quad (2.18)$$

on the far-field in conjunction with a sponge zone (Bodony 2006) which smoothly ramps the solution towards the asymptotic solution in an enlarged computational domain. The difference between the current state vector $\boldsymbol{q}^{(i+1)}$ and a reference state $\boldsymbol{q}_r$ spatially weighted by some function

$$\sigma=\frac{c\,\Psi}{\sqrt{Re}} \quad (2.19)$$

is introduced as a source term in (2.13) for that purpose. The divisor $\sqrt{Re}$ ensures constant local weighting in the space-marching procedure while c is a constant weight factor. A function $\boldsymbol{\Psi} : \mathbb{R}^2 \to [0, 1]^2$ separates the sponge region from the physical solution and uses a fifth-order polynomial to smoothly ramp the source-term influence from zero at the beginning of the sponge zone (denoted by subscript s) up to its full magnitude on the far-field boundary (subscript max). In preliminary simulations it was found sufficient to enforce the far-field boundary-parallel cross-flow velocity w_1 in order to converge the flow field to close agreement with the self-similar solution for large Reynolds numbers. This observation leads to the following choice for $\boldsymbol{q}_r$ and $\boldsymbol{\Psi}$:

$$\boldsymbol{q}_r = [0, 0, w_1, w_1, 0]^{\mathrm{T}}, \tag{2.20}$$

$$\boldsymbol{\Psi} = [0, 0, \boldsymbol{\Psi}_v, \boldsymbol{\Psi}_w, 0]^{\mathrm{T}}, \tag{2.21}$$

$$\boldsymbol{\Psi}_v = \begin{cases} 6\tilde{y}^5 - 15\tilde{y}^4 + 10\tilde{y}^3 & \text{for } y_s \leqslant y \leqslant y_{max} \\ 0 & \text{for } y < y_s \end{cases} \tag{2.22a}$$

$$\boldsymbol{\Psi}_w = \begin{cases} 6\tilde{z}^5 - 15\tilde{z}^4 + 10\tilde{z}^3 & \text{for } z_s \leqslant z \leqslant z_{max} \\ 0 & \text{for } z < z_s \end{cases} \tag{2.22b}$$

with $\tilde{y} = (y - y_s)/y_{max}$, $\tilde{z} = (z - z_s)/z_{max}$. The velocity w_1 is calculated as the secondary compressible cross-flow induced by superposition of the displacement effects of two perpendicular flat plates. In the limit of a large distance from the opposing wall, w_1 is governed by the cross-flow momentum equation

$$\mu_0 \frac{\mathrm{d}^2 w_1}{\mathrm{d}\eta^2} + \left[\frac{\mathrm{d}\mu_0}{\mathrm{d}\eta} + \rho_0(\eta u_0 - v_1)\right] \frac{\mathrm{d}w_1}{\mathrm{d}\eta} + \rho_0 u_0 w_1 = \beta_1 \tag{2.23}$$

subject to the boundary conditions

$$w_1(0) = 0, \quad w_1(\eta \to \infty) = \beta_1 \tag{2.24}$$

where

$$\beta_1 = \int_0^\infty 1 - \frac{u_0}{T_0} \mathrm{d}\eta \tag{2.25}$$

is a constant related to the displacement thickness and

$$\eta = \frac{y^*}{\sqrt{2}x^*} \sqrt{Re_x} \tag{2.26}$$

the similarity coordinate. Here, we follow Ghia & Davis (1974*a*) who derived (2.23) using first higher-order potential flow approximations for the cross-flow pressure gradient in the corresponding momentum equation. An asterisk * indicates dimensional values and Re_x is the Reynolds number based on the dimensional distance from the leading edge. ρ_0, u_0, v_1 and μ_0 comprise solutions to the classical flat-plate boundary-layer problem for a general compressible fluid. The enforcement of the asymptotic cross-flow through a sponge region was found to yield better convergence characteristics than direct enforcement via non-homogeneous Dirichlet boundary conditions. It also allows the flow a certain deviation from the self-similar solution in regions where the latter is not applicable, e.g. close to the leading edge at the beginning of the integration.

The flow field is initialized with its free stream values $\boldsymbol{q}_{x=0} = [\rho_\infty, u_\infty, 0, 0, T_\infty]^{\mathrm{T}}$ corresponding to a state upstream of the leading edge with downstream influence of

the corner walls neglected. The linear system (2.11) is now advanced in space given the initial conditions.

2.3. *Numerical method*

The use of spectral methods in fluid mechanical applications was pioneered in the early 1970s by Kreiss & Oliger (1972) and Orszag & Patterson (1972). Details on the various methods are given in the books by Canuto *et al.* (1988), Boyd & Boyd (2001) or Trefethen (2000). The corner-flow problem is solved using a pseudo-spectral Chebyshev–Chebyshev collocation method in the transversal planes. In the pseudospectral methodology, partial derivatives are replaced by the corresponding differentiation matrices

$$\frac{\partial \boldsymbol{q}}{\partial y} = \boldsymbol{D_y q}, \quad \frac{\partial \boldsymbol{q}}{\partial z} = \boldsymbol{D_z q}, \tag{2.27}$$

whose entries are given by algebraic relations (e.g. Trefethen 2000). A computational grid of dimension $N \times N$ is constructed from Gauss–Lobatto points

$$\hat{y}_j = \hat{z}_j = \cos\frac{j\pi}{N}, \quad j = 1, 2, \ldots, N \tag{2.28}$$

which comprise the extrema of the Nth-order Chebyshev polynomial defined by $T_N(y) = \cos(N \cos^{-1} y)$ on the interval $[-1, 1]$. This choice of points is optimal in terms of accuracy of the method. However, the grid clustering going along with the cosinusoidal point distribution is advantageous only near the wall where large gradients in the solution are expected. For the far-field region, a wider grid spacing is favoured. A transformation of the form

$$y = a\frac{1+\hat{y}}{b-\hat{y}}, \quad a = \frac{y_i y_{max}}{y_{max} - 2y_i}, \quad b = 1 + \frac{2a}{y_{max}} \tag{2.29}$$

serves this purpose (z-direction treated in an analogous manner). Equations (2.29) transforms the Gauss–Lobatto grid defined on $[-1, 1]$ to the physical domain $[0, y_{max}]$ and allows for a clustering of one half of the grid points to the interval $[0, y_i]$ (Schmid & Henningson 2001).

2.4. *Base-flow results*

The laminar corner-flow problem was solved for three different Mach numbers representing the incompressible limit ($Ma = 0.01$), subsonic ($Ma = 0.95$) and supersonic ($Ma = 1.5$) flow respectively. The lower Mach number cases were calculated on a 35×35 and the supersonic case on a 40×40 collocation point grid with $y_{max} = 45$, $y_s = z_s = 0.75 y_{max}$ and $y_i = y_{max}/25$. The spatial integration step was set to $\Delta x = 0.02/\delta_1$ for the incompressible limit, $\Delta x = 0.0002/\delta_1$ for the subsonic and $\Delta x = 0.000\,15/\delta_1$ for the supersonic case. It was observed that the solution converges to the self-similar solution for higher Reynolds numbers with the second-order asymptotic cross-flow enforced as described in § 2.2. Comparisons between the PNS and the self-similar solution from the pioneering work by Weinberg & Rubin (1972) are presented in figure 2. Good agreement was found for all three Mach numbers for the streamwise (a) and cross-flow (b) velocities along the corner bisector. The isolines of the cross-flow velocity v are depicted in (c) for the supersonic case at a local Reynolds number of 1585. They show a local maximum on the corner bisector and a jet-like cross-flow profile close to the wall at $z = 0$ as typical for the corner-flow problem. The profiles of streamwise velocity, density and temperature are generally in

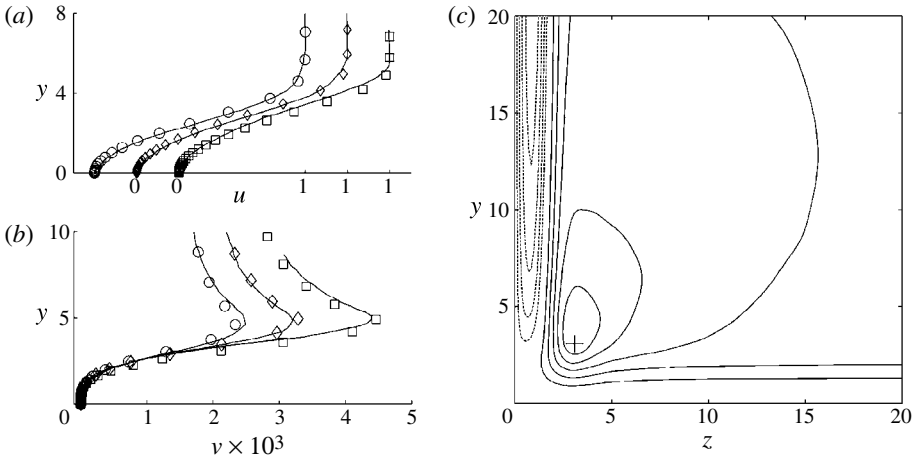

FIGURE 2. (*a*) and (*b*) Velocity profiles along symmetry line: (lines) self-similar solution of Weinberg & Rubin (1972), (○) PNS for $Ma = 0.01$, (◇) PNS for $Ma = 0.95$, (□) PNS for $Ma = 1.5$; (*a*) streamwise velocity u, (*b*) cross-flow velocity v. (*c*) Isolines of cross-flow velocity v in the transversal plane at $Re = 1585$ and $Ma = 1.5$: (solid lines) $v > 0$, (dashed lines) $v < 0$, (+) $v = v_{max}$.

very good agreement with their one-dimensional self-similar flat-plate counterparts. Pressure fluctuations induced by the instant enforcement of the no-slip boundary condition in the first integration step are minimized by linearly ramping $y_{max} = z_{max}$ from 10 to the final domain height during the first 75 ($Ma = 0.01$, $Ma = 0.95$) or 300 ($Ma = 1.5$) space steps.

Interestingly, the present PNS approach is confronted with a Mach number limit of $Ma \approx 2$ above which no stable solution was obtained. The same observation was made for the self-similar solution by Weinberg & Rubin (1972) and elaborated in further detail by Mikhail & Ghia (1978).

3. Linear stability

A very detailed description of the formalism and history of linear stability is given by Mack (1984) who pioneered the compressible branch of the theory. Two-dimensional LST is comprehensively summarized by Theofilis (2003). The general approach is shortly reviewed in the following § 3.1.

3.1. *Stability equations*

The Navier–Stokes equations are linearized by decomposition of the flow quantities in a time varying perturbation $\boldsymbol{q}'$ and a steady primary state $\boldsymbol{q}_0$ which satisfies the Navier–Stokes equations itself:

$$\boldsymbol{q}(x, y, z, t) = \boldsymbol{q}_0(x, y, z) + \boldsymbol{q}'(x, y, z, t). \tag{3.1}$$

Under the assumption of parallel flow and small perturbations of the normal mode form

$$\boldsymbol{q}'(x, y, z, t) = \hat{\boldsymbol{q}}(y, z) \cdot \mathrm{e}^{\mathrm{i}(\alpha x - \omega t)}, \tag{3.2}$$

the problem is reduced to a generalized eigenvalue problem of the form

$$\mathscr{A}\hat{\boldsymbol{q}} = \omega \mathscr{B}\hat{\boldsymbol{q}}. \tag{3.3}$$

In the above, $\hat{\boldsymbol{q}}$ is the eigenvector of the eigenvalue problem formed by the coefficient matrices $\mathscr{A}$ and $\mathscr{B}$, α streamwise wavenumber and ω the complex-valued angular frequency. Temporal growth of infinitesimally small disturbances is attested to solutions with $\mathrm{Im}(\omega) > 0$. Details on the treatment of pressure perturbation terms and terms containing spatial derivatives of the perturbation viscosity can be found in Groskopf, Kloker & Marxen (2010). The entries of the coefficient matrices $\mathscr{A}$ and $\mathscr{B}$ are derived analogous to their one-dimensional counterparts as can be found in Mack (1984).

3.2. *Boundary conditions*

At solid walls, zero velocity and temperature fluctuations are assumed

$$\hat{u} = \hat{v} = \hat{w} = \hat{T} = 0 \tag{3.4}$$

with no boundary condition necessary for the perturbation density. Sommerfeld's radiation condition

$$\frac{\partial \hat{\boldsymbol{q}}}{\partial n} = \mathrm{i}\beta \hat{\boldsymbol{q}} \tag{3.5}$$

permits specification of a phase angle given by $\tan^{-1}(\beta/\alpha)$ on far-field boundaries (Parker & Balachandar 1999). This leads to the formation of oblique travelling waves. A positive value of β is associated with waves travelling away from the corner bisector while negative values of β indicate incoming waves. Choosing $\beta = 0$ corresponds to enforcing a standing wave pattern. The phase angle $\tan^{-1}(\beta/\alpha)$ enforced by (3.5) and the spanwise wavenumbers β dictated by the domain extent $y_{max} = z_{max}$ are not compatible in general as the latter is not known *a priori* and varies within the spectrum. Incompatibility leads to deformations of the eigenfields towards the far-field boundaries. This topic is further addressed in §§ 3.4.2 and 3.4.3.

3.3. *Numerical method*

A Krylov subspace-based shift and invert Arnoldi algorithm is used to solve the large eigenvalue problem posed by (3.3). ARPACK routines (Lehoucq, Sorensen & Yang 1998) are employed for this purpose. Base-flow results were interpolated on the stability grid using cubic spline interpolation.

3.3.1. *Computational grid and domain size*

A thorough study on grid refinement and the influence of the domain extent on amplification rates has been undertaken by Parker & Balachandar (1999) for incompressible self-similar corner flow. Following these authors the domain size was set to $y_{max} = 29$ corresponding to $\eta = 35$ if not stated otherwise to guarantee proper resolution of the viscous modes. The grid transformation by means of (2.29) allows for a significant reduction of collocation points by densifying grid points towards the walls where the instability modes are active. A value of $y_i = y_{max}/5$ was found best suited for most parameter combinations in this regard. Figure 3 shows an example of a spectrum at $Re = 980$, $Ma = 0.95$, $\alpha = 0.2$, $\beta = 0$, $y_{max} = 29$ and $y_i = y_{max}/5$ for four different numbers of collocation points. Here $c = \mathrm{Re}(\omega)/\alpha$ is the perturbation phase speed and $\mathrm{Im}(\omega)$ the amplification rate. A total of 25 modes were calculated using the shift and invert Arnoldi algorithm for each resolution. The arc-shaped line-up of eigenvalues corresponds to the continuous branch of Tollmien–Schlichting (TS) modes with differing spanwise wavenumbers. The spanwise wavenumber cannot be enforced directly by means of the domain size as the extent of the perturbation field area

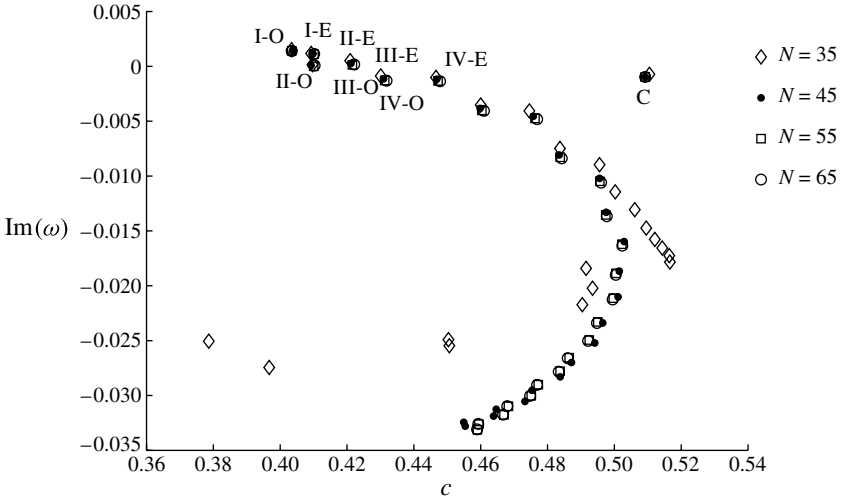

FIGURE 3. Eigenvalue spectrum for $Re = 980$, $Ma = 0.95$, $\alpha = 0.2$, $\beta = 0$, $y_i = y_{max}/5$: ($\diamond$) $N = 35$, ($\bullet$) $N = 45$, ($\square$) $N = 55$, ($\circ$) $N = 65$; Latin numbers indicate increasing spanwise wavenumbers, (-E) even/symmetric TS modes, (-O) odd/antisymmetric TS modes and (C) corner mode.

influenced by the corner is not known in advance. Therefore, modes are not identified by their exact spanwise wavenumber. Instead, Latin numbers distinguish modes of increasing spanwise wavenumbers, i.e.1/4 (I), 3/4 (II), and 1 (III) waves are resolved in the computational domain. We refer to mode I as to the fundamental mode. -O indicates odd or antisymmetric and -E indicates even or symmetric mode shape with respect to the corner bisector. The inviscid corner mode is denoted by C. More examples of the modal structure are given in the § 3.4. Good correspondence of the eigenvalues can be seen for $N = 65$, $N = 55$ and $N = 45$ in the upper half plane of the spectrum. Eigenvalues calculated with $N = 35$ depart from their higher resolved counterparts even for low spanwise wavenumbers.

The eigenvalue convergence of the four leading viscous modes and the inviscid corner mode is further investigated in figure 4. An absolute error defined as the difference to the solution obtained at the highest resolution under consideration ($N = 65$) is plotted against the number of collocation points N for the growth rate $\Delta\mathrm{Im}(\omega)$ (a) and the phase speed Δc (b). It can be seen that no significant improvement of accuracy is achieved by increasing the number of collocation points beyond $N = 45$. The phase speed error shows a comparable behaviour for $N \geqslant 40$. A resolution of $N \approx 65$ is required for comparable convergence without grid clustering by means of (2.29). This leads us to the choice of $N = 45$ for the following calculations if not stated otherwise.

3.4. *Linear stability results*

The basic features of the modal corner-flow stability problem are reviewed in § 3.4.1. The following § 3.4.2 is concerned with the influence of wave obliqueness on temporal amplification rates. The neutral stability in three-dimensional parameter space spanned by Re, α and β is addressed in § 3.4.3. Finally, some remarks on the appearance and form of acoustic modes in the supersonic regime are given in § 3.4.4.

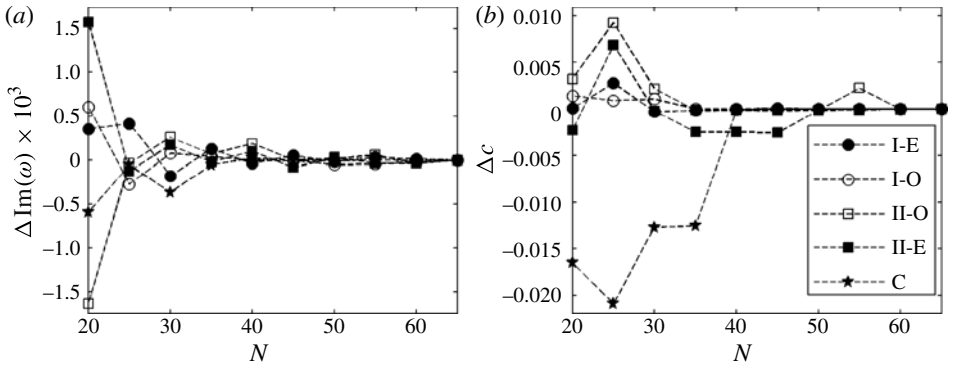

FIGURE 4. Convergence of growth rate (a) and phase speed (b) of the four leading viscous modes and the corner mode for $Re = 980$, $Ma = 0.95$, $\alpha = 0.2$, $\beta = 0$, $y_i = y_{max}/5$ in terms of the difference to the solution obtained at $N = 65$: $\Delta\mathrm{Im}(\omega) = \mathrm{Im}(\omega(N) - \omega(N = 65))$, $\Delta c = \mathrm{Re}(\omega(N) - \omega(N = 65))/\alpha$, (solid symbols, -E) even/symmetric TS modes, (empty symbols, -O) odd/antisymmetric TS modes, Latin numbers indicate increasing spanwise wavenumbers, ($\star$, C) corner mode.

3.4.1. *Spectra and eigenfields*

The basic structure of the corner-flow spectrum resembles that of the flat-plate scenario with some additional modes active in the corner region only. The latter modes appear distinct in the spectrum while TS-type instabilities form continuous branches rendered discrete by the restriction to certain wavelengths through the finite extent of the computational domain.

The fundamental TS branch can be seen in figure 3. TS modes appear in pairs of even- and odd-symmetry with respect to the corner bisector. While all viscous modes appear in pairs of even- and odd-symmetric, no odd-symmetric equivalent of the corner mode is observed in the subsonic regime. The spatial structure of an odd-symmetric (a) and the inviscid corner mode (b) are visualized in figure 5 by means of streamwise velocity contours. It can be seen that the influence of the corner is spatially restricted to its close vicinity. As the wave obliqueness angle is enforced on the far-field boundaries, no influence on the inviscid corner mode can be expected.

3.4.2. *Wave obliqueness and temporal amplification*

The influence of wave obliqueness on corner-flow stability was first considered by Parker & Balachandar (1999) and later by Galionis & Hall (2005) in their study of the incompressible spatial stability problem using the parabolized stability equations.

The spatial structure of incoming (a) and outgoing (b) oblique waves is visualized in figure 6 by contours of the streamwise velocity component at a constant distance $z = 1$ from the lower wall in the y, t-plane. The spatiotemporal structures clearly reveal the oblique nature of the disturbances. Disturbances enter the computational domain through the far-field boundary at $y = y_{max}$ for the case with $\beta < 0$ (a) and leave the domain part (b) with $\beta > 0$. Temporal decay is observed in both cases.

Figures 7, 8 and 9 show the modal dependence of temporal amplification on β for $Ma = 0.01$, $Ma = 0.95$ and $Ma = 1.5$, respectively, at the critical Reynolds number and corresponding spanwise wavenumber of the one-dimensional far-field profiles with zero spanwise wavenumber. For each value of β, 20 eigensolutions were calculated using the implicitly restarted Arnoldi algorithm around the solution of the corresponding one-dimensional far-field stability problem. Cross-correlation of

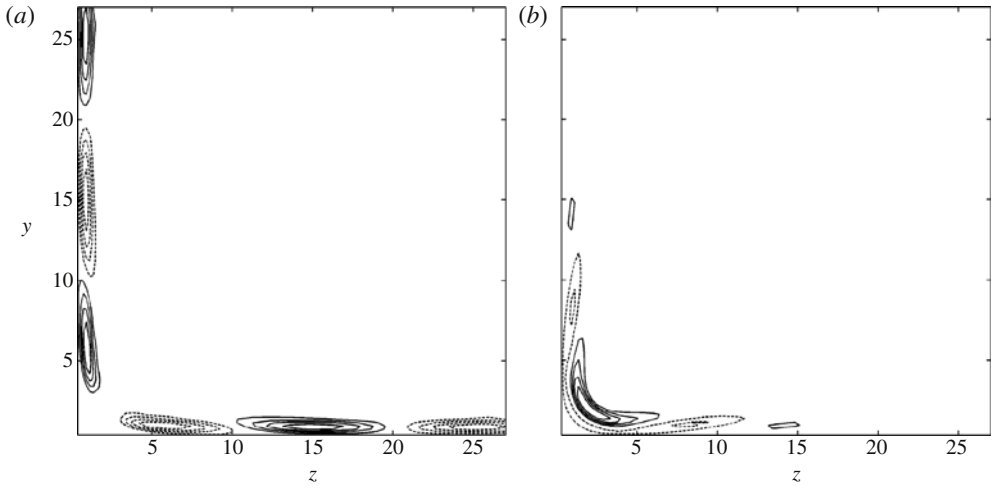

FIGURE 5. Eigenfields of the streamwise perturbation velocity $\hat{u}$ for $Re = 602$, $Ma = 0.95$, $\alpha = 0.245$, $\beta = -0.85$; (solid lines) $\hat{u} > 0$, (dashed lines) $\hat{u} < 0$: (*a*) real part of mode III-O, (*b*) real part of corner mode C.

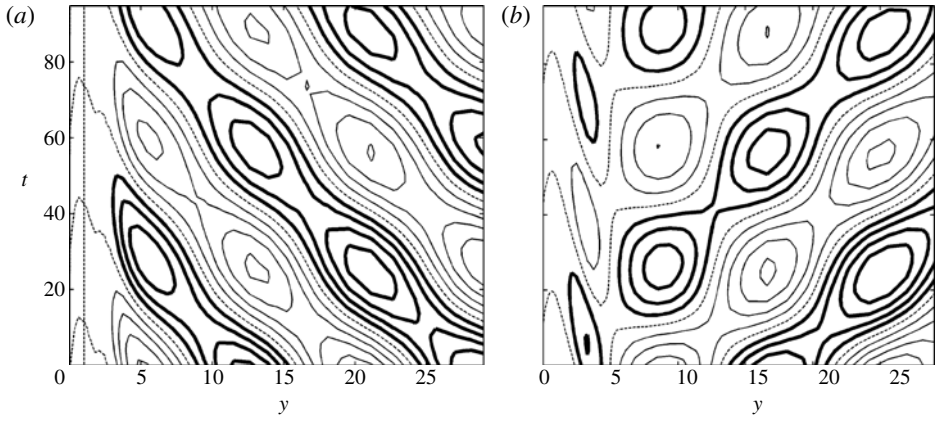

FIGURE 6. Temporal evolution of streamwise perturbation velocity contours over 1.5 periods for $Re = 1373$, $Ma = 0.95$, $\alpha = 0.2$ at constant wall distance $z = 1$; (thick lines) $\hat{u} > 0$, (thin lines) $\hat{u} < 0$, (dashed line) $\hat{u} = 0$: (*a*) incoming oblique waves of mode IV-O for $\beta = -0.5$, (*b*) outgoing oblique waves of mode IV-E for $\beta = 0.0745$.

the eigenfunctions was used for mode tracking. Parts (*a*) of each figure show the spectra for the corresponding Mach number at $\beta = -0.85$. Figure 7 reproduces the findings by Parker & Balachandar (1999) for the incompressible limit. Growth rates of disturbances travelling towards the opposing wall are enhanced while waves travelling away from the wall are suppressed. The maximum modal growth rate is observed to occur at lower values of β with increasing spanwise wave number. Also, the overall effect of β on amplification rates by means of the difference between modal maxima and minima increases with spanwise wavenumber. The extrema indicate the proper values of β for compatibility between modal spanwise wavelength and the far-field phase angle imposed by (3.5) for incoming (maxima) and outgoing (minima)

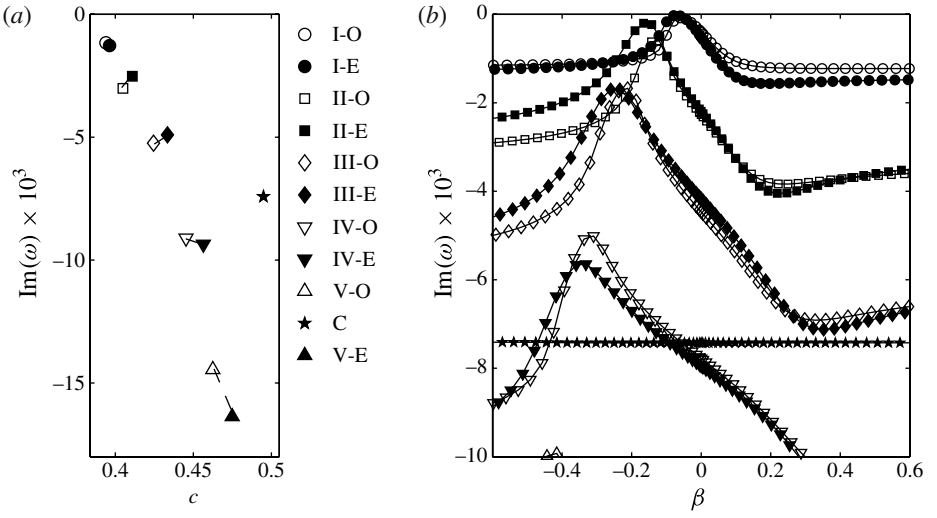

FIGURE 7. Dependence of temporal amplification on β for $Ma = 0.01$, $\alpha = 0.3$ at the critical Reynolds number of the one-dimensional far-field with $\beta = 0$; (solid symbols, -E) even/symmetric TS modes, (empty symbols, -O) odd/antisymmetric TS modes, Latin numbers indicate increasing spanwise wavenumbers, (dashed lines) connect even/odd mode pairs of equal spanwise wave number, ($\star$, C) corner mode: (*a*) spectrum, (*b*) modal growth rates ω_i over spanwise wavenumber β.

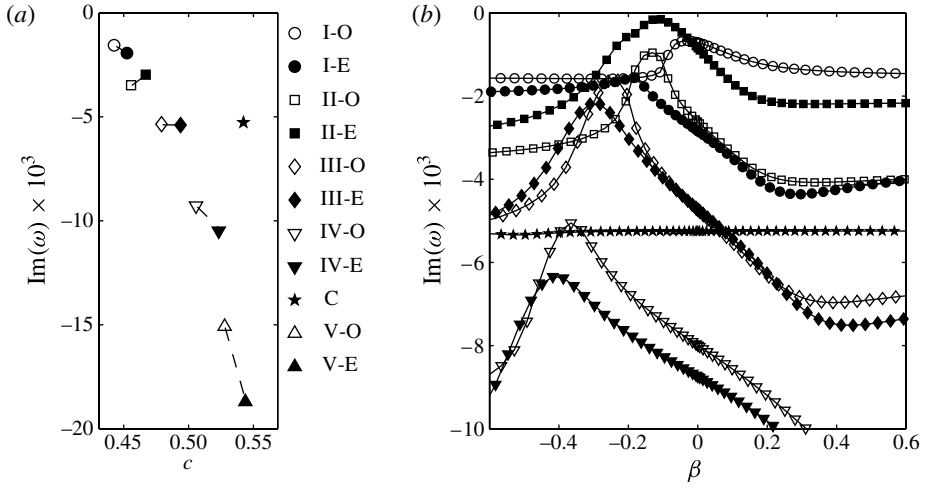

FIGURE 8. Same as figure 7, but for $Ma = 0.95$, $\alpha = 0.245$.

disturbances. Different amplification rates of outgoing and incoming disturbances of the same spanwise wavelength can be explained by the break of symmetry through the corner as opposed to the flat-plate scenario where no such distinction exists (Parker & Balachandar 1999). As presumed, the corner mode exhibits no dependence on the obliqueness angle enforced at the far-field. Similar general trends are observed for the $Ma = 0.95$ case (figure 8). In all three cases, the overall maximum amplification rate is found somewhat close to the one of the one-dimensional far-field for $\beta = 0$.

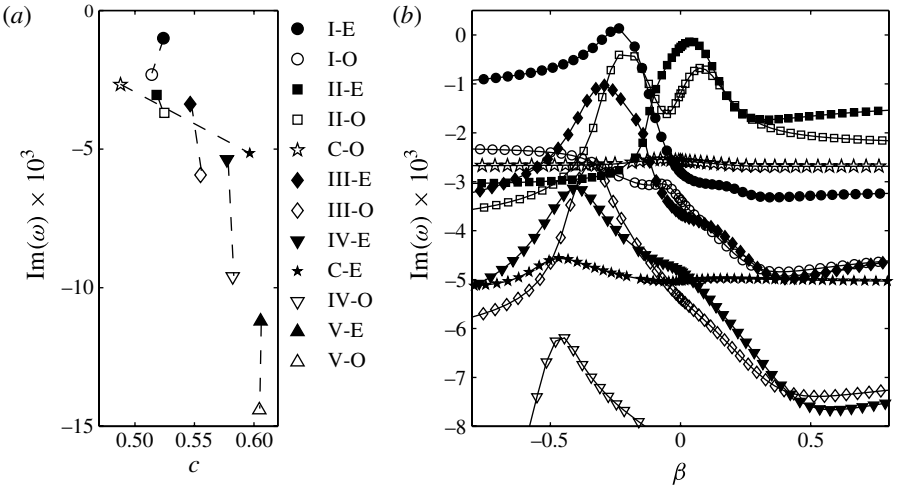

FIGURE 9. Same as figure 7, but for $Ma = 1.5$, $\alpha = 0.19$.

The supersonic flow case as shown in figure 9 exhibits an additional mode which is not present in the subsonic cases. It comprises an antisymmetric counterpart to the inviscid corner mode. Visualizations of the even (*a*) and odd (*b*) symmetric corner mode by means of temporal isosurfaces of the streamwise perturbation velocity are presented in figure 10. The calculation with the highest growth rate of the even-symmetric corner mode corresponding to $\beta = -0.25$ at $Re = 699$ is used for visualization. It can be seen from figure 10(*a*) that the even mode is no longer spatially restricted to the vicinity of the corner, hereby revealing viscous properties. Starting at some distance from the corner a transitions towards wave-like patterns of some distinct spanwise wavenumber as common for the viscous instability is observed. This effect is also indicated by the emerging dependence of the growth rate on β with its maximum at $\beta \approx -0.5$ (compare figure 9(*b*), symbol $\star$). The odd-symmetric corner mode possesses a globally higher amplification rate almost independent on β.

3.4.3. *Neutral stability and critical Reynolds number*

Neutral stability curves for the six most amplified modes of the TS branch and the corner mode are depicted in figure 11 for a fixed value of $\beta = 0$ at $Ma = 0.95$. Neutral refers to the state of zero amplification, i.e. isolines of $\mathrm{Im}(\omega) = 0$. The neutral stability curve of the one-dimensional far-field flow is given as a reference (dashed line). It can be seen that the pairs of even and odd modes possess comparable neutral curves for the fundamental TS wave and the first higher harmonic. The corner mode exhibits a higher critical Reynolds number in comparison with the fundamental TS wave.

However, the critical Reynolds number for the compressible corner-flow problem for a given Mach number is located somewhere in the three-dimensional parameter space spanned by Reynolds number Re, streamwise wavenumber α and phase angle $\tan^{-1}(\beta/\alpha)$ or spanwise wavenumber β accordingly. The latter can only be fixed indirectly via the extent of the computational domain. The following stability analysis is restricted to discrete spectra with distinct spanwise wavenumbers predetermined by the fixed computational domain size. In order to estimate the critical parameters equation (3.3) was solved for all combinations of 15 Reynolds numbers, 15 values of α and 18 values of β resulting in a total of 4050 calculations for each

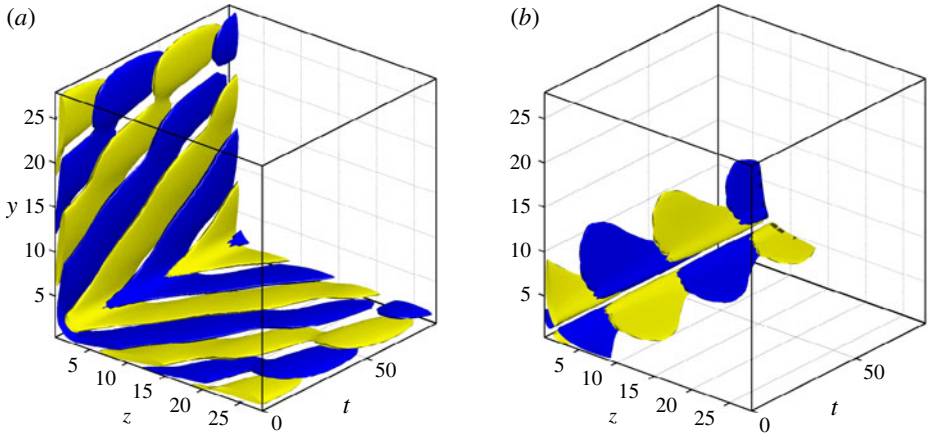

FIGURE 10. (Colour online available at journals.cambridge.org/flm) Eigenfields of streamwise perturbation velocity $\hat{u}$ for the even-symmetric (*a*) and odd-symmetric (*b*) corner mode at $Re = 699$, $Ma = 1.5$, $\alpha = 0.19$, $\beta = -0.25$: (blue) $\hat{u} = -0.75\hat{u}_{max}$, (yellow) $\hat{u} = 0.75\hat{u}_{max}$.

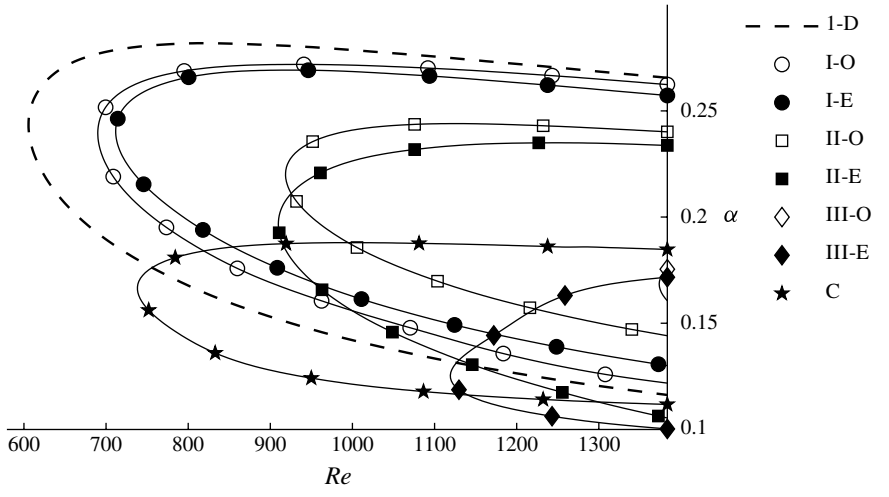

FIGURE 11. Stability diagram for $Ma = 0.95$, $\beta = 0$; (solid symbols, -E) even/symmetric TS modes, (empty symbols, -O) odd/antisymmetric TS modes, ($\star$, C) corner mode, Latin numbers indicate increasing spanwise wavenumbers, (dashed line) one-dimensional far-field.

Mach number. The parameter space was chosen $Re, \alpha, \beta \in [500,\ 800] \times [0.15,\ 0.375] \times [-0.45,\ 0.1]$ for $Ma = 0.01$, $Re, \alpha, \beta \in [550,\ 850] \times [0.13,\ 0.29] \times [-0.45,\ 0.1]$ for $Ma = 0.95$ and $Re, \alpha, \beta \in [650,\ 1000] \times [0.1,\ 0.22] \times [-0.45,\ 0.1]$ for $Ma = 1.5$. The problem of finding the appropriate phase angle to be enforced via the far-field boundary condition for each spanwise wavenumber is addressed by taking this approach. Neutral surfaces were extracted and interpolated on a finer grid using cubic spline interpolation to extract the critical parameters listed in table 1. The critical Reynolds number and streamwise wavenumber decrease with increasing Mach numbers while no clear trend can be deduced for the critical value of β. In all three

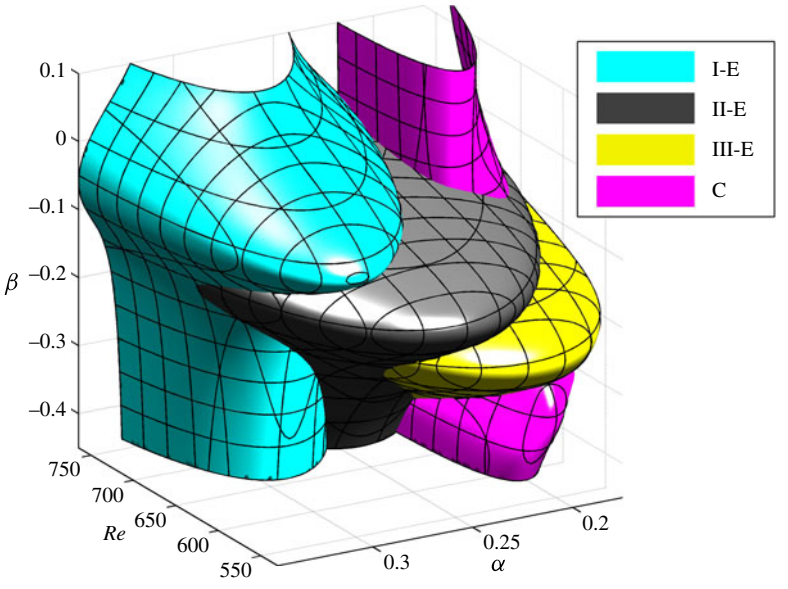

FIGURE 12. (Colour online) Isometric view of neutral surfaces of different modes for $Ma = 0.01$: (cyan) I-E, (grey) II-E, (yellow) III-E and (magenta) C.

Ma	Re_{crit}	α_{crit}	β_{crit}	Mode
0.01	551	0.260	−0.161	II-E
0.95	611	0.240	−0.117	II-E
1.50	668	0.175	−0.256	II-E

TABLE 1. Critical values of Re, α and β determined from the neutral stability surfaces for $Ma = 0.01$, $Ma = 0.95$ and $Ma = 1.5$.

Mach number cases, the first even harmonic (II-E) of the TS branch was identified as the critical mode. This result is notable as it contradicts the expectation deduced from the limiting flat plate scenario for incompressible flow where a two-dimensional wave is most amplified according to Squire's theorem. Here, the mode with the lowest spanwise wavenumber permitted by the computational domain extent possesses the highest amplification rate. We suggest two possible explanations. Physically, the break of symmetry through the opposing wall can lead to a lower amplification rate as compared to the periodic case with $\beta = 0$. Second, numerical damping through the far-field boundary condition can not be ruled out as a possible cause. In addition, the effect of domain truncation as elaborated by Parker & Balachandar (1999) has to be mentioned.

Cross-correlation of the eigenfunctions was successfully applied to separate modes in the three-dimensional parameter space for the $Ma = 0.01$ case. Neutral stability surfaces of the first three even modes and the corner mode are presented in figure 12. The critical values occurring for mode II-E (grey) correspond to the values given in table 1. The critical value of β for each mode decreases with increasing streamwise wavenumber. The onset of viscous behaviour of the corner mode (magenta) for negative values of β as described in § 3.4.2 is observed for the incompressible case

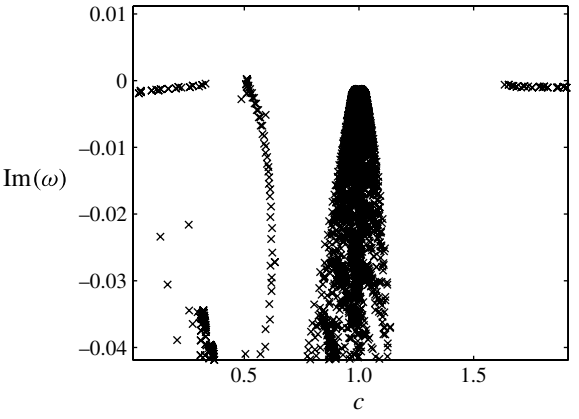

FIGURE 13. Eigenvalue spectrum for $Re = 699$, $Ma = 1.5$, $\alpha = 0.19$, $\beta = 0$, $N = 60$, $y_i = y_{max}/8$ and $y_{max} = 80$.

as well. The neutral stability surface of the corner mode is almost independent of β for $\beta > -0.01$. All modes share the property that their individual critical point occurs at some negative value of β, i.e. for incoming waves.

3.4.4. *Acoustic modes*

Unlike in the incompressible case, acoustic disturbance modes are present in supersonic corner flow. In general, acoustic modes in boundary-layer-type flows can be divided in fast and slow travelling modes of phase speed

$$c = 1 \pm \frac{1}{Ma}. \tag{3.6}$$

Figure 13 shows a part of the full spectrum calculated using QZ factorization for $Ma = 1.5$. The flow state was chosen as that of the neutral point of the corresponding one-dimensional far-field. The domain size had to be extended to $y_{max} = 80$ to cover the maxima of some acoustic waves. Insufficient domain size led to overpredicted amplification rates for the acoustic modes in previous calculations. This behaviour is typically observed for acoustic disturbances in boundary-layer-type flows, i.e. by Hanifi, Schmid & Henningson (1996) for the flat-plate scenario. The number of collocation points was increased to $N = 60$ to guarantee proper spatial resolution. As the domain extent of the LST calculation exceeds that of the PNS solution the base flow was extrapolated onto the enlarged domain assuming constant asymptotic values

$$\boldsymbol{q}(y, z)|_{y>y_{max} \vee z>z_{max}} = \begin{cases} \boldsymbol{q}(y_{max}, z) & \text{for } y > y_{max} \wedge z \leqslant z_{max} \\ \boldsymbol{q}(y, z_{max}) & \text{for } y \leqslant y_{max} \wedge z > z_{max} \\ \boldsymbol{q}(y_{max}, z_{max}) & \text{for } y > y_{max} \wedge z > z_{max}. \end{cases} \tag{3.7}$$

No disturbance of the eigenfields was observed as a result of the extrapolation. The continuous spectrum vertically located at $c \approx 1$ is the most prominent feature present in the figure. The fundamental TS branch can be seen at $0.5 \lesssim c \lesssim 0.6$, flanked by the even- (right, $c \approx 0.6$) and odd-symmetric (left, $c \approx 0.5$) corner mode. Two highly dampened higher harmonic TS branches are also distinguishable at $c \approx 0.4$. Slow travelling acoustic modes form a horizontal branch with phase speeds $c \lesssim 0.33$ while fast travelling modes are found at $c \gtrsim 1.67$ in accordance with (3.6).

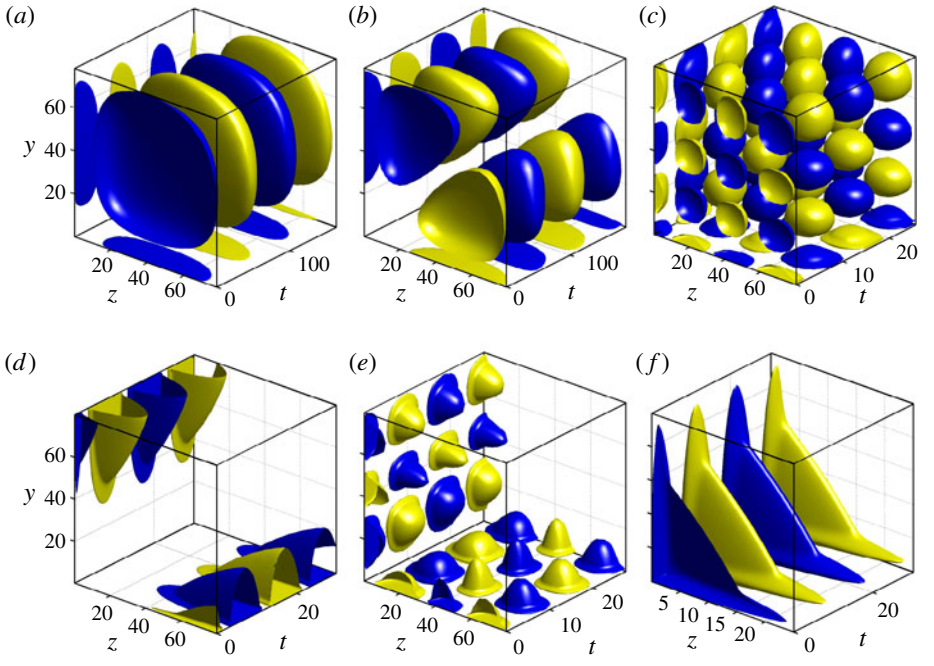

FIGURE 14. (Colour online) Isosurfaces of the streamwise perturbation velocity $\hat{u}$ for $Re = 699$, $Ma = 1.5$, $\alpha = 0.19$, $\beta = 0$, $N = 60$, $y_i = y_{max}/8$ and $y_{max} = 80$ (blue, $\hat{u} = -0.75\hat{u}_{max}$; yellow, $\hat{u} = 0.75\hat{u}_{max}$): (*a*) even fast acoustic mode, (*b*) odd fast acoustic mode, (*c*) even slow acoustic mode, (*d*) fundamental and (*e*) higher harmonic wall-bounded slow acoustic modes, (*f*) slow even acoustic corner mode.

Visualizations by means of isosurfaces of some representative acoustic modes are depicted in figure 14. The modes presented can be separated into even- (14*a*,*c*,*f*) and odd-symmetric (14*b*,*d*,*e*), wall-bounded (14*d*–*f*), and non-wall-bounded (14*a*–*c*), as well as slow (14*c*–*f*), and fast (14*a*,*b*). In contrast to the TS and corner modes, even wall-bounded acoustic modes expand far into the potential flow far-field. An acoustic corner mode (14*f*) of rapidly decaying perturbation amplitude away from the corner was identified within the slowly travelling acoustic branch of the spectrum (note the reduced transversal plane scale of 14*f* to one quarter of part 14*a*–*e*). All acoustic modes observed for the $Ma = 1.5$ case were damped. It is known from the flat-plate scenario (Fedorov 2003) that acoustic modes become an important facet in stability and transition when boundary-layer and acoustic modes synchronize at higher Mach numbers.

4. Summary and outlook

The study at hand complements the existing knowledge on the incompressible linear stability characteristics of the streamwise corner-flow problem by extending the analysis to the compressible regime. Special attention has been paid to the appropriate treatment of wave obliqueness to extract the critical values of Reynolds number, streamwise wavenumber and spanwise wavenumber. The modal stability analysis predicts perturbations similar to those active in the flat-plate boundary layer, i.e. TS waves. They appear in pairs of odd- and even-symmetric modes with respect to the corner bisector and form branches of distinct spanwise wavenumbers.

As each spanwise wavenumber necessitates the corresponding phase angle to be adequately imposed on far-field boundaries, we have expanded the linear stability analysis by one parameter and extracted the critical values from neutral surfaces in the three-dimensional parameter space. Results for three representative Mach numbers have been compared. They show a general trend of increasing critical displacement-thickness-based Reynolds number and decreasing critical streamwise wavenumber with increasing Mach number, comparable to the flat-plate boundary layer. No such trend is found for the critical spanwise wavenumber. An odd-symmetric corner mode is identified for the case of supersonic free stream conditions which is not observed in the subsonic regime. Notably, it exceeds the growth rate of its even-symmetric counterpart also present in the spectrum. In addition, the supersonic corner-flow spectrum includes slow and fast travelling acoustic modes of even- and odd-symmetry. Among them an acoustic corner mode is found.

Unfortunately, no validation with experimental data is possible as no such data exists as a consequence of the difficulty in establishing a steady and symmetric corner flow in experiment without imposing a favourable pressure gradient. Prospectively, an extension of the analysis to higher Mach numbers is desirable as inviscid mechanisms comparable to those active on a single flat plate as described by Mack (1984) are very likely to be encountered. It is not yet clear whether the discrepancy of one order of magnitude in the critical Reynolds number between theory and experiment stems from experimental shortcomings. Another hypothesis is a different transition mechanism not yet identified. Following this line, Galionis & Hall (2005) suggest a nonlinear mechanism through the interaction of higher harmonics and various viscous modes while an inviscid mechanism or large transient growth is brought into the discussion by Alizard *et al.* (2010). An investigation of the full three-dimensional, non-parallel and nonlinear problem by means of direct numerical simulation is currently in progress.

REFERENCES

ALIZARD, F., ROBINET, J.-C. & RIST, U. 2010 Sensitivity analysis of a streamwise corner flow. *Phys. Fluids* **22** (1).

BALACHANDAR, S. & MALIK, M. R. 1993 Inviscid instability of streamwise corner flow. NASA STI/Recon Technical Report Number 94.

BARCLAY, W. H. 1973 Experimental investigation of the laminar flow along a straight 135-deg corner. *Aeronaut. Q.* **24**, 147–154.

BARCLAY, W. H. & EL-GAMAL, H. A. 1983 Streamwise corner flow with wall suction. *AIAA J.* **21**, 31–37.

BARCLAY, W. H. & EL-GAMAL, H. A. 1984 Further solutions in streamwise corner flow with wall suction. *AIAA J.* **22**, 1169–1171.

BARCLAY, W. H. & RIDHA, A. H. 1980 Flow in streamwise corners of arbitrary angle. *AIAA J.* **18**, 1413–1420.

BODONY, D. J. 2006 Analysis of sponge zones for computational fluid mechanics. *J. Comput. Phys.* **212**, 681–702.

BOYD, J. P. & BOYD, J. P. 2001 *Chebyshev and Fourier Spectral Methods*. Dover.

CANUTO, C., HUSSAINI, M. Y., QUARTERONI, A. & ZANG, T. A. 1988 *Spectral Methods in Fluid Dynamics*. Springer.

CARRIER, G. 1947 The boundary layer in a corner. *Q. Appl. Maths* **4**, 367–370.

DAVIS, T. A. 2006 *Direct Methods for Sparse Linear Systems*. Society for Industrial Mathematics.

DHANAK, M. R. 1992 Instability of flow in a streamwise corner. *ICASE Report* No. 92-70.

DHANAK, M. R. 1993 On the instability of flow in a streamwise corner. *Proc. R. Soc. Lond.* A **441**, 201–210.

DUCK, P. W. & DHANAK, M. R. 1996 The effects of free stream pressure gradient on a corner boundary layer. *APS Meeting Abstracts*.

EL-GAMAL, H. A. & BARCLAY, W. H. 1978 Experiments on the laminar flow in a rectangular streamwise corner. *Aeronaut. Q.* **29**, 75–97.

FEDOROV, A. V. 2003 Receptivity of a high-speed boundary layer to acoustic disturbances. *J. Fluid Mech.* **491**, 101–129.

GALIONIS, I. & HALL, P. 2005 Spatial stability of the incompressible corner flow. *Theor. Comput. Fluid Dyn.* **19**, 77–113.

GHIA, K. N. 1975 Incompressible streamwise flow along an unbounded corner. *AIAA J.* **13**, 902–907.

GHIA, K. N. & DAVIS, R. T. 1974*a* A study of compressible potential and asymptotic viscous flows for corner region. *AIAA J.* **12**, 355–359.

GHIA, K. N. & DAVIS, R. T. 1974*b* Corner layer flow: optimization of numerical method of solution. *Comput. Fluids* **2**, 17–34.

GROSKOPF, G., KLOKER, M. J. & MARXEN, O. 2010 Bi-global crossplane stability analysis of high-speed boundary-layer flows with discrete roughness. In *Seventh IUTAM Symposium on Laminar–Turbulent Transition* (ed. P. Schlatter & D. S. Henningson), pp. 171.

HANIFI, A., SCHMID, P. J. & HENNINGSON, D. S. 1996 Transient growth in compressible boundary layer flow. *Phys. Fluids* **8**, 826–837.

KREISS, H. O. & OLIGER, J. 1972 Comparison of accurate methods for the integration of hyperbolic equations. *Tellus* **24** (3), 199–215.

LAKIN, W. D. & HUSSAINI, M. Y. 1984 Stability of the laminar boundary layer in a streamwise corner. *Proc. R. Soc. Lond.* A **393**, 101–116.

LEHOUCQ, R. B., SORENSEN, D. C. & YANG, C. 1998 *ARPACK Users' Guide: Solution of Large-Scale Eigenvalue Problems with Implicitly Restarted Arnoldi Methods*. SIAM.

MACK, L. M. 1984 Boundary-layer linear stability theory. In *AGARD Special Course on the Stability and Transition of Laminar Flow*.

MIKHAIL, A. G. & GHIA, K. N. 1978 Viscous compressible flow in the boundary region of an axial corner. *AIAA J.* **16**, 931–939.

NOMURA, Y. 1962 Theoretical and experimental investigations on the incompressible viscous flow around the corner. *Mem. Defence Acad. Japan* **2**, 115–145.

NOMURA, Y. 1982 Analysis of a characteristic of laminar corner flow. *AIAA J.* **20**, 1020–1022.

ORSZAG, S. & PATTERSON, G. 1972 Numerical simulation of turbulence. *Statist. Model Turbul.* 127–147.

PAL, A. & RUBIN, S. G. 1971 Asymptotic features of viscous flow along a corner. *Q. Appl. Maths* **29**, 91–108.

PARKER, S. J. & BALACHANDAR, S. 1999 Viscous and inviscid instabilities of flow along a streamwise corner. *Theor. Comput. Fluid Dyn.* **13**, 231–270.

RIDHA, A. 1992 On the dual solutions associated with boundary-layer equations in a corner. *J. Engng Maths* **26**, 525–537.

RIDHA, A. 2002 Combined free and forced convection in a corner. *Intl J. Heat Mass Transfer* **45** (10), 2191–2205.

RUBIN, S. G. 1966 Incompressible flow along a corner. *J. Fluid Mech. Digital Archive* **26** (01), 97–110.

RUBIN, S. G. & GROSSMAN, B. 1971 Viscous flow along a corner: numerical solution of the corner layer equations. *Q. Appl. Maths* **29**, 169–186.

RUBIN, S. G. & TANNEHILL, J. C. 1992 Parabolized/reduced Navier–Stokes computational techniques. *Annu. Rev. Fluid Mech.* **24**, 117–144.

SCHMID, P. J. & HENNINGSON, D. S. 2001 *Stability and Transition in Shear Flows*. Springer.

TANNEHILL, J., ANDERSON, D. & PLETCHER, R. 1997 *Computational Fluid Mechanics and Heat Transfer*. Taylor & Francis.

THEOFILIS, V. 2003 Advances in global linear instability analysis of nonparallel and three-dimensional flows. *Prog. Aeronaut. Sci.* **39**, 249–315.

TREFETHEN, LLOYD N. 2000 *Spectral Methods in MATLAB*. Society for Industrial Mathematics.

WEINBERG, B. C. & RUBIN, S. G. 1972 Compressible corner flow. *J. Fluid Mech.* **56**, 753–774.

ZAMIR, M. 1970 Boundary-layer theory and the flow in a streamwise corner (Flow equations for curvilinear boundary layer based on laminar incompressible boundary layer in streamwise corner). *Aeronaut. J.* **74**, 330–332.

ZAMIR, M. 1981 Similarity and stability of the laminar boundary layer in a streamwise corner. *Proc. R. Soc. Lond.* A **377**, 269–288.

ZAMIR, M. & YOUNG, A. D. 1970 Experimental investigation of the boundary layer in a streamwise corner. *Aeronaut. Q.* **30**, 471–484.

ZAMIR, M. & YOUNG, A. D. 1979 Pressure gradient and leading edge effects on the corner boundary layer. *Aeronaut. Q.* **30**, 471–483.